

# Molecular-level study on the role of methanesulfonic acid in iodine oxoacids nucleation

Jing Li<sup>1</sup>, Nan Wu<sup>1</sup>, **Biwu Chu<sup>2,3</sup>**, An Ning<sup>1,\*</sup>, and Xiuhui Zhang<sup>1,\*</sup>

<sup>1</sup>Key Laboratory of Cluster Science, Ministry of Education of China, School of Chemistry and Chemical Engineering, Beijing Institute of Technology, Beijing, 100081, China

<sup>2</sup>State Key Joint Laboratory of Environment Simulation and Pollution Control, Research Center for Eco-Environmental Sciences, Chinese Academy of Sciences, Beijing, 100085, China

<sup>3</sup>College of Resources and Environment, University of Chinese Academy of Sciences, Beijing, 100049, China

*Correspondence to:* A. Ning (anning@bit.edu.cn) and X.H. Zhang (zhangxiuhui@bit.edu.cn)

**Abstract.** Iodic acid (HIO<sub>3</sub>) and iodous acid (HIO<sub>2</sub>) have been identified to nucleate effectively by the Cosmics Leaving OUtdoor Droplets (CLOUD) experiment at CERN, yet it may be hard to explain all HIO<sub>3</sub>-induced nucleation. Given the complexity of marine atmosphere, other precursors may be involved. Methanesulfonic acid (MSA), as a widespread precursor over oceans, has been proven to play a vital role in facilitating nucleation. However, its kinetic impacts on the synergistic nucleation of iodine oxoacids remain unclear. Hence, we investigated the MSA-involved HIO<sub>3</sub>-HIO<sub>2</sub> nucleation process at the molecular level using density functional theory (DFT) and Atmospheric Clusters Dynamic Code (ACDC). **Our results show that MSA can form stable molecular clusters with HIO<sub>3</sub> and HIO<sub>2</sub> jointed via hydrogen bond, halogen bond, and electrostatic attraction after proton transfer to HIO<sub>2</sub>.** Thermodynamically, the MSA-involved clustering can occur nearly without free-energy barrier, following the HIO<sub>2</sub>-MSA binary and HIO<sub>3</sub>-HIO<sub>2</sub>-MSA ternary pathway. **Furthermore, our results show that considering MSA will significantly enhance the calculated rate of HIO<sub>3</sub>-HIO<sub>2</sub>-based cluster formation, with up to 10<sup>4</sup>-fold at cold marine regions containing rich MSA and scarce iodine, such as polar Ny-Ålesund and Marambio.** Thus, the proposed more efficient HIO<sub>3</sub>-HIO<sub>2</sub>-MSA nucleation mechanism may provide theoretical evidence for explaining the frequent and intensive **bursts** of marine iodine particles.

## 1 Introduction

Marine aerosol, which is the primary natural aerosol (O'Dowd and Leeuw, 2007), has a significant impact on global climate, radiation balance, and even human health (Wang et al., 2010; Pöschl, 2005). New particle formation (NPF) is a primary source of marine aerosols, which proceeds via nucleation and subsequent growth (Lee et al., 2019; Zhang, 2010; Kulmala et al., 2013; Zhang et al., 2012). **Moreover**, the nucleation, forming critical clusters at 1-2 nm from gaseous precursors, is the pivotal step affecting NPF (Zhang, 2010; Kulmala et al., 2013). However, the chemicals involved in nucleation and the underlying mechanisms remain poorly understood, due to technological limitations in the molecular-level analysis. Additionally, the lack of comprehensive and long-term ocean observations, further hinders our knowledge of marine NPF.

Recent field studies suggest that marine NPF events are closely related to atmospheric iodine-bearing molecules emitted by algae (Yu et al., 2019; Baccarini et al., 2020; Beck et al., 2021). During the NPF events in coastal (e.g., Mace Head and Zhejiang) (Sipilä et al., 2016; Yu et al., 2019) and polar oceans (e.g., Arctic Ocean) (Baccarini et al., 2020), the nucleation processes are mainly driven by iodic acids ( $\text{HIO}_3$ ). However, the self-nucleation of  $\text{HIO}_3$  alone cannot fully explain the observed NPF rates (Rong et al., 2020). More recently, the Cosmics Leaving OUtdoor Droplets (CLOUD) experiment at CERN has found that iodous acid ( $\text{HIO}_2$ ) plays a key role in stabilizing  $\text{HIO}_3$ , enabling effective nucleation by the sequential addition of  $\text{HIO}_3$  followed by  $\text{HIO}_2$  (He et al., 2021). Further theoretical studies uncover that the stabilizing effect of  $\text{HIO}_2$  on  $\text{HIO}_3$  stems from its role as a base in clustering (Zhang et al., 2022b; Liu et al., 2023). Although the efficient nucleation of  $\text{HIO}_3$  and  $\text{HIO}_2$  is overall consistent with the CLOUD measurement (Zhang et al., 2022a), this mechanism does not account for all  $\text{HIO}_3$ -induced nucleation in the authentic atmosphere (Ma et al., 2023). Thus, other essential precursors in the marine atmosphere might potentially affect  $\text{HIO}_3$ - $\text{HIO}_2$  nucleation, but which and how remain largely unexamined.

Methanesulfonic acid (MSA), as a typical marine sulfur precursor, is widespread over oceans (Saltzman et al., 1983; Read et al., 2008; Chen et al., 2012; Yan et al., 2019) with considerable atmospheric concentrations ( $10^5 - 10^8 \text{ molec. cm}^{-3}$ ) (Eisele and Tanner, 1993; Dal Maso et al., 2002; Chen et al., 2018; Yan et al., 2019). Moreover, MSA has been shown to initiate nucleation with vital atmospheric precursors, such as ammonia and amines, enhancing cluster formation (O'Dowd et al., 2002; Bork et al., 2014; Shen et al., 2019; Shen et al., 2020; Brean et al., 2021; Liu et al., 2022). Importantly, current evidence suggests that MSA can also form stable clusters with  $\text{HIO}_3$  or  $\text{HIO}_2$  individually, but none of the resulting binary nucleation can explain field measurements well (Ning et al., 2022; Wu et al., 2023). Despite the stabilizing effect of MSA on iodine oxoacids, it remains unknown whether MSA can synergistically nucleate with  $\text{HIO}_3$  and  $\text{HIO}_2$ , as well as the induced kinetic impacts on clustering. Furthermore, given the coexistence of MSA and  $\text{HIO}_3$  in different marine regions (Quéléver et al., 2022; Beck et al., 2021), along with the consistent presence of  $\text{HIO}_3$  and  $\text{HIO}_2$  as homologous substances (Sipilä et al., 2016), the importance of the  $\text{HIO}_3$ - $\text{HIO}_2$ -MSA nucleation mechanism may differ under distinct ambient conditions, but it remains unrevealed.

Herein, we have systematically investigated the  $\text{HIO}_3$ - $\text{HIO}_2$ -based nucleation involved in MSA, including  $(\text{HIO}_3)_x(\text{HIO}_2)_y(\text{MSA})_z$  ( $1 \leq x + y + z \leq 5$ ,  $0 \leq z \leq 3$ ) clusters, by combining quantum chemical (QC) approach and Atmospheric Clusters Dynamic Code (ACDC) (McGrath et al., 2012). To probe the nature of cluster formation, the wavefunction analysis was performed to investigate the intermolecular interactions. And the Gibbs free energies of cluster formation were calculated to evaluate cluster stability. Moreover, a series of ACDC simulations were executed to delve into the influence of MSA on nucleation rates and mechanisms under varying atmospheric conditions, such as precursor concentration and temperature.

**2.1 Quantum Chemistry Calculations**

To locate the low-lying isomers of  $(\text{HIO}_3)_x(\text{HIO}_2)_y(\text{MSA})_z$  ( $1 \leq x + y + z \leq 5$ ,  $0 \leq z \leq 3$ ) clusters, the multi-step conformer search was adopted here (details in Supporting Information (SI)). The resulting stable clusters with the lowest energies were identified at  $\omega\text{B97X-D}/6\text{-}311++\text{G}(3\text{df},3\text{pd})$  (for C, H, O, and S atoms) + aug-cc-pVTZ-PP with ECP28MDF (for I atom) level of theory (Francl et al., 1982; Peterson et al., 2003), and the corresponding Cartesian coordinates were collected in Table S9. In addition, the structures of pure-HIO<sub>3</sub>, pure-HIO<sub>2</sub>, pure-MSA, HIO<sub>3</sub>-HIO<sub>2</sub>, HIO<sub>3</sub>-MSA, and HIO<sub>2</sub>-MSA clusters in the present study were adopted from the previous studies (Rong et al., 2020; Zhang et al., 2022b; Liu et al., 2023; Ning et al., 2022; Wu et al., 2023). All density functional theory (DFT) calculations were carried out using the Gaussian 09 package (Frisch et al., 2009), where FineGrid and tight convergence were employed. The single-point energy was calculated at the RI-CC2/aug-cc-pVTZ (for C, H, and O atoms) + aug-cc-pV(T+d)Z (for S atom) + aug-cc-pVTZ-PP with ECP28MDF (for I atom) level of theory (Hättig and Weigend, 2000) by TURBOMOLE program (Ahlich et al., 1989), because of its success in fitting with the experiments (Lu et al., 2020; Kürten et al., 2018; Rong et al., 2020; Almeida et al., 2013). In the present study, the Gibbs formation free energy ( $\Delta G_{\text{ref}}$ , kcal mol<sup>-1</sup>) of the HIO<sub>3</sub>-HIO<sub>2</sub>-MSA clusters at the reference pressure (1 atm) was calculated as:

$$\Delta G_{\text{ref}} = \Delta E_{\text{RI-CC2}} + \Delta G_{\text{thermal}}^{\omega\text{B97X-D}}, \quad (1)$$

where  $\Delta E_{\text{RI-CC2}}$  is the electronic contribution and  $\Delta G_{\text{thermal}}^{\omega\text{B97X-D}}$  is the thermal contribution to free energy. The  $\Delta G_{\text{ref}}$  at different temperatures ( $T = 258 - 298$  K) were calculated using the Shermo 2.0 code (Lu and Chen, 2021) and collected in Table S1. Further given the effect of vapor pressures of the precursor, the  $\Delta G_{\text{ref}}$  was converted to  $\Delta G(P_1, P_2, \dots, P_n)$  (Vehkamäki, 2006) by the Eq. (2):

$$\Delta G(P_1, P_2, \dots, P_n) = \Delta G_{\text{ref}} - k_{\text{B}}T \sum_{i=1}^n N_i \ln\left(\frac{P_i}{P_{\text{ref}}}\right), \quad (2)$$

where  $n$  is the number of components within the cluster,  $k_{\text{B}}$  denotes the Boltzmann constant,  $T$  signifies the temperature,  $N_i$  refers to the number of molecules of type  $i$  in the number of components in the cluster, and  $P_i$  is the partial pressure of component  $i$  in the vapor phase.

**2.2 Wavefunction Analysis**

Wavefunction analysis was carried out using Multiwfn 3.7 (Lu and Chen, 2012) to investigate the binding nature within molecular clusters. The electrostatic potential (ESP) on the van der Waals (vdW) surface was calculated to identify active interaction sites. Specifically, the negative ESP region is electron-rich, while the positive ESP region is electron-deficient, potentially leading to mutual non-covalent interactions, such as hydrogen bonds (HBs) and halogen bonds (XBs). To further quantify the bond strength, the electron density  $\rho(r)$ , Laplacian electron density  $\nabla^2\rho(r)$ , and energy density  $H(r)$  at bond critical points (BCPs) were calculated based on the atoms in molecules (AIM) theory (Lane et al., 2013).

## 90 2.3 Atmospheric Clusters Dynamic Simulations

To explore nucleation kinetic, the Atmospheric cluster dynamics code (ACDC) (McGrath et al., 2012) was adopted here to compute the cluster formation rates, steady-state concentrations, and formation pathways by explicit solution of the birth-death equations (Eq. (3)).

$$\frac{dC_i}{dt} = \frac{1}{2} \sum_{j < i} \beta_{j,(i-j)} C_j C_{(i-j)} + \sum_j \gamma_{(i+j) \rightarrow i} C_{i+j} - \sum_j \beta_{i,j} C_i C_j - \frac{1}{2} \sum_{j < i} \gamma_{i \rightarrow j} C_i + Q_i - S_i, \quad (3)$$

95 where the subscripts ( $i, j, i-j$  and  $i+j$ ) denote different clusters or monomers,  $C_i$  is the concentration of cluster  $i$ ,  $\beta_{i,j}$  and  $\gamma_{(i+j) \rightarrow i}$  represent the cluster collision and evaporation rate coefficient, respectively. And  $Q_i$  and  $S_i$  denote the external source and sink terms, respectively. The  $\beta_{i,j}$  is calculated as follows:

$$\beta_{i,j} = \left(\frac{3}{4\pi}\right)^{1/6} \left(\frac{6k_B T}{m_i} + \frac{6k_B T}{m_j}\right)^{1/2} (V_i^{1/3} + V_j^{1/3})^2, \quad (4)$$

100 where  $m_i$  and  $V_i$  represent the mass and volume of cluster  $i$ , respectively. And  $V_i = 3/4 \times \pi \times (d_i/2)^3$ , where the diameter  $d_i$  of cluster  $i$  is derived from the cluster volume  $V_i$  calculated by Multiwfn 3.7 (Lu and Chen, 2012). The  $\gamma_{(i+j) \rightarrow i}$  is calculated by the Eq. (5):

$$\gamma_{(i+j) \rightarrow i} = \beta_{i,j} \frac{P_{\text{ref}}}{k_B T} \exp\left(\frac{\Delta G_{i+j} - \Delta G_i - \Delta G_j}{k_B T}\right), \quad (5)$$

where  $P_{\text{ref}}$  is the reference pressure at 1 atm, and  $\Delta G$  is the formation free energy of the cluster.

105 In the performed ACDC simulations, we considered all possible collision and evaporation processes, including monomer-monomer, monomer-cluster and cluster-cluster collisions, as well as decomposition of parent clusters into monomers and clusters, or into two smaller clusters. Additionally, whether the clusters in the simulated system are stable depends on whether the rate of collision frequencies exceeds the total evaporation rate coefficients ( $\beta C / \Sigma \gamma > 1$ ) (Table S4). The setting of the boundary conditions of ACDC simulations is summarized in Table S3. The uncertainty analysis was performed in this study (Table S8 and Figs. S15, S16 and S17), with details provided in Supporting Information (SI).

## 110 3 Results and Discussion

Here, conformational analysis was first carried out to study how MSA affects intermolecular interactions in the HIO<sub>3</sub>-HIO<sub>2</sub>-MSA clusters. And the thermodynamic analysis was employed to assess stability of the formed clusters. To gain insights into nucleation mechanisms, a series of ACDC simulations were executed under varying atmospheric conditions.

### 3.1 Cluster Conformational Analysis

115 Strong interactions among nucleation precursors are pivotal for forming stable clusters. To evaluate the binding potential of MSA with HIO<sub>3</sub> and HIO<sub>2</sub>, we calculated the ESP-mapped molecular vdW surface to identify interaction sites. As illustrated

in Fig. 1, MSA has a positive ESP maximum (+63.95 kcal mol<sup>-1</sup>) at the H atom of its -OH group, serving as a HB donor. The iodine atoms of HIO<sub>3</sub> and HIO<sub>2</sub> with positive ESP maximums (+51.90 and +45.26 kcal mol<sup>-1</sup>), can act as XB donors. Additionally, the oxygen atoms in the S=O group (from MSA) and I=O group (from HIO<sub>3</sub> and HIO<sub>2</sub>) with strong electronegativity can act as HB or XB acceptor sites, due to the lone pair electrons. Therefore, as shown in Fig. 1(d), MSA, HIO<sub>3</sub>, and HIO<sub>2</sub> have the potential to form clusters via intermolecular HBs and XBs.

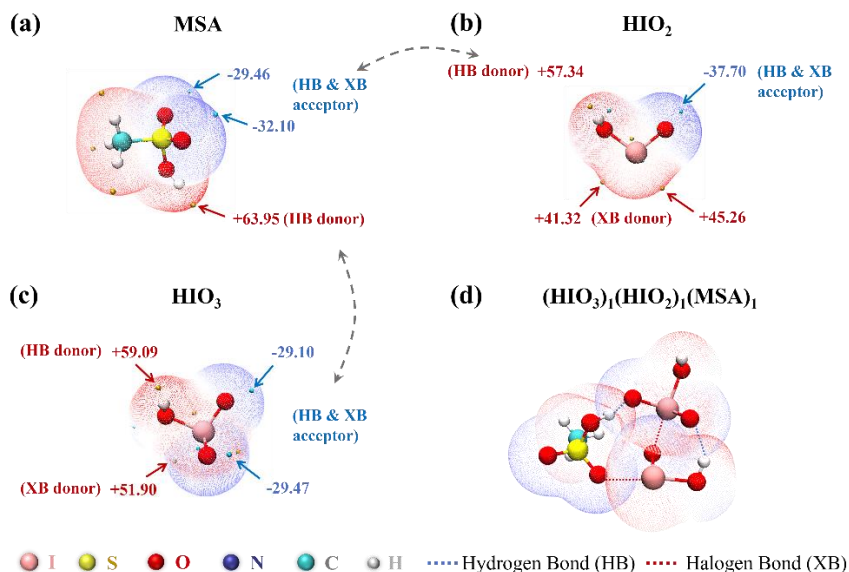


**Figure 1.** The ESP-mapped molecular vdW surface of (a) MSA, (b) HIO<sub>2</sub>, (c) HIO<sub>3</sub> and (d) (HIO<sub>3</sub>)<sub>1</sub>(HIO<sub>2</sub>)<sub>1</sub>(MSA)<sub>1</sub>. The golden and cyan dots represent the positions of maximums and minimums of ESP (unit: kcal mol<sup>-1</sup>), respectively. The gray dashed arrows signify the site-to-site interaction tendencies.

As presented in Fig. 2, all the identified HIO<sub>3</sub>-HIO<sub>2</sub>-MSA clusters are structurally stabilized by the network of HBs (blue dashed lines) and XBs (red dashed lines). Within these clusters, the inward-facing oxygen atom and hydroxyl (-OH) group in MSA facilitates its being involved in forming more HBs and XBs, compared to the HIO<sub>3</sub>-HIO<sub>2</sub> clusters (Fig. S1). Statistically, within HIO<sub>3</sub>-HIO<sub>2</sub>-MSA clusters, the percentage of XBs (61%) is higher than that of HBs (39%). Notably, during the HIO<sub>3</sub>-HIO<sub>2</sub>-MSA cluster formation, HIO<sub>2</sub> behaves like a base and is protonated by MSA instead of HIO<sub>3</sub>, likely due to **stronger** acidity of MSA than HIO<sub>3</sub>. After the MSA-driven proton transfer to HIO<sub>2</sub>, the resulting electrostatic interactions between the formed ion pairs (CH<sub>3</sub>SO<sub>3</sub><sup>-</sup> - H<sub>2</sub>IO<sub>2</sub><sup>+</sup>) further stabilize the clusters. Taken together, MSA can form clusters with HIO<sub>3</sub> and HIO<sub>2</sub> via HBs, XBs, and electrostatic attraction between ion pairs after proton transfer. Additionally, taking the (HIO<sub>3</sub>)<sub>1</sub>(HIO<sub>2</sub>)<sub>3</sub>(MSA)<sub>1</sub> cluster for example, there are still some potential remaining unoccupied binding sites as shown in Fig. S2. It suggests that the studied large-size clusters still have unoccupied HB and XB sites that can potentially facilitate the condensation of precursors in the atmosphere, enhancing further growth of marine aerosols.

To further quantify bond strength within HIO<sub>3</sub>-HIO<sub>2</sub>-MSA clusters, the topological analysis was performed based on the atoms in molecules (AIM) theory. The electron density  $\rho(r)$ , Laplacian electron density  $\nabla^2\rho(r)$ , and energy density  $H(r)$  at the corresponding bond critical points (BCPs) in the studied HIO<sub>3</sub>-HIO<sub>2</sub>-MSA clusters were calculated and collected in Table S2. The  $\rho(r)$  is generally positively associated with the bond strength. For the HIO<sub>3</sub>-HIO<sub>2</sub>-MSA clusters,  $\rho(r)$  values at the BCPs of the HBs range from 0.0090 to 0.0869 a.u., exceeding the reported threshold of HB (0.002 – 0.040 a.u.) (Koch and Popelier, 1995; Grabowski, 2004). Moreover, the associated values of  $\nabla^2\rho(r)$  at these BCPs range from 0.0310 to 0.1180 a.u., falling within the suggested range for HB (0.014 – 0.139 a.u.) (Koch and Popelier, 1995; Grabowski, 2004). Meanwhile, for O–I···O XBs, the  $\rho(r)$  and  $\nabla^2\rho(r)$  values within HIO<sub>3</sub>-HIO<sub>2</sub>-MSA clusters range from 0.0068 to 0.1999 a.u. and 0.0288 to 0.1744 a.u., respectively. Collectively, MSA can stabilize HIO<sub>3</sub>-HIO<sub>2</sub> clusters via more relatively strong HBs and XBs, while also protonating HIO<sub>2</sub> to form ion pairs.

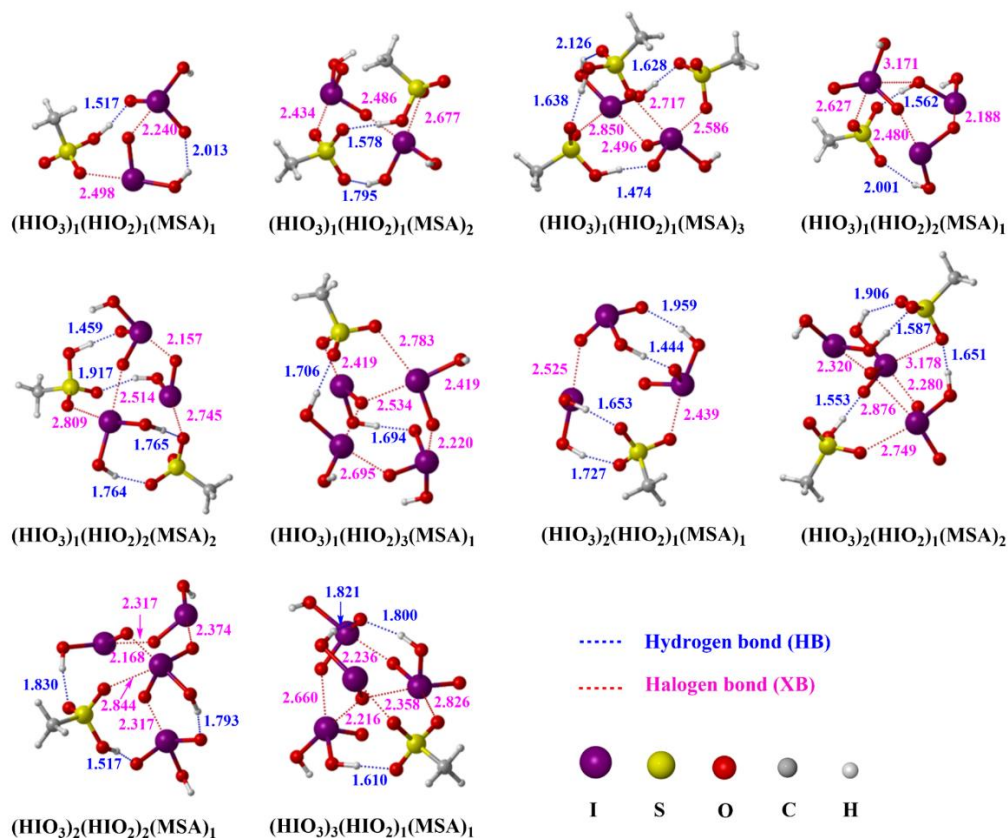


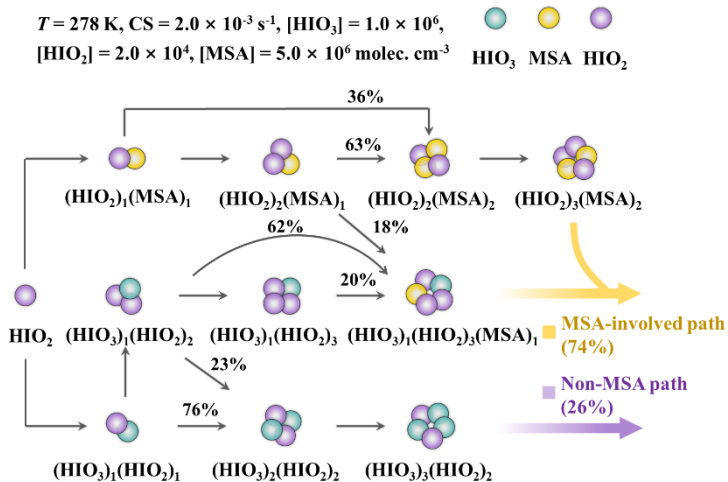
**Figure 2.** The most stable configurations of the HIO<sub>3</sub>-HIO<sub>2</sub>-MSA ternary clusters identified at the  $\omega$ B97XD/6-311++G(3df, 3pd) (for C, H, O, and S atoms) + aug-cc-pVTZ-PP with ECP28MDF (for I atom) level of theory. The lengths of bonds are given in Å.

### 150 3.2 Cluster Formation Pathways and Free Energy Surface

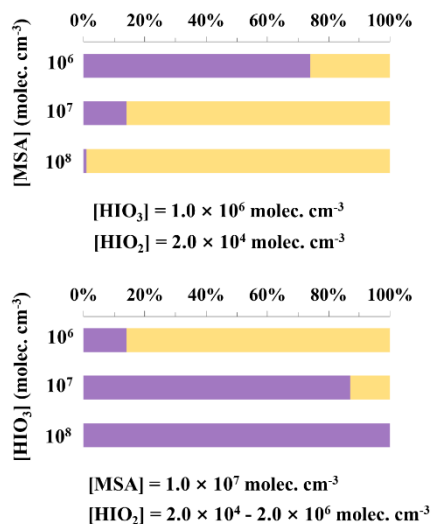
To explore how MSA affects HIO<sub>3</sub>-HIO<sub>2</sub>-based nucleation kinetic, the ACDC simulations were employed to reveal the nucleation mechanism under varying atmospheric conditions. Based on the field measurement (Berresheim et al., 2002; Chen et al., 2018; Sipilä et al., 2016; Beck et al., 2021), the ranges of [MSA], [HIO<sub>3</sub>], and [HIO<sub>2</sub>] are set to be 10<sup>6</sup> – 10<sup>8</sup>, 10<sup>6</sup> – 10<sup>8</sup> and 2.0 × 10<sup>4</sup> – 2.0 × 10<sup>6</sup> molec. cm<sup>-3</sup>, respectively, where [HIO<sub>3</sub>]/[HIO<sub>2</sub>] is a constant. Here, the condensation sink (CS) coefficient is set to be 2.0 × 10<sup>-3</sup> s<sup>-1</sup> (Dal Maso et al., 2002) and the temperature (*T*) is 278 K. Under such conditions, the molecular-level nucleation pathways and the corresponding branching ratios are depicted in Fig. 3(a). The detailed branch ratio is also shown at 278 K (Fig. S3) and 268 K (Fig. S4). Furthermore, to comprehend how the growth occurs thermodynamically, we herein calculated the Gibbs free energies ( $\Delta G$ , Eq. (2)) along the main clustering pathway at the conditions of *T* = 268 – 278 K, [HIO<sub>3</sub>] = 1.0 × 10<sup>6</sup>, [HIO<sub>2</sub>] = 2.0 × 10<sup>4</sup>, and [MSA] = 5.0 × 10<sup>6</sup> molec. cm<sup>-3</sup> (Fig. 3(b) and Fig. S5).

As shown in Fig. 3(a), the clustering pathways, at *T* = 278 K, CS = 2.0 × 10<sup>-3</sup> s<sup>-1</sup>, [HIO<sub>3</sub>] = 1.0 × 10<sup>6</sup>, [HIO<sub>2</sub>] = 2.0 × 10<sup>4</sup>, and [MSA] = 5.0 × 10<sup>6</sup> molec. cm<sup>-3</sup>, can be categorized into two main types: i) MSA-involved pathways, including HIO<sub>2</sub>-MSA and HIO<sub>3</sub>-HIO<sub>2</sub>-MSA nucleation; and ii) non-MSA pathways, primarily involving HIO<sub>3</sub>-HIO<sub>2</sub> nucleation. For the HIO<sub>2</sub>-MSA pathway, the initial formation of (HIO<sub>2</sub>)<sub>1</sub>(MSA)<sub>1</sub> heterodimer occurs without any energy barrier (Fig. 3(b)). And the subsequent cluster growth mainly proceeds via sequential addition of HIO<sub>2</sub> or MSA monomer, partly coupled with cluster collisions. Specifically, 63% of (HIO<sub>2</sub>)<sub>2</sub>(MSA)<sub>2</sub> results from (HIO<sub>2</sub>)<sub>2</sub>(MSA)<sub>1</sub> colliding with MSA monomer with an energy barrier of 1.00 kcal mol<sup>-1</sup>, while 36% from a barrierless combination of two (HIO<sub>2</sub>)<sub>1</sub>(MSA)<sub>1</sub> cluster. At this point, kinetic drives growth by colliding (HIO<sub>2</sub>)<sub>2</sub>(MSA)<sub>1</sub> with MSA monomer, instead of following the lowest energy pathway. This is because the collision frequency of (HIO<sub>2</sub>)<sub>1</sub>(MSA)<sub>1</sub> and a HIO<sub>2</sub> monomer is relatively higher, stemming from the higher [HIO<sub>2</sub>]. Then, the formed (HIO<sub>2</sub>)<sub>2</sub>(MSA)<sub>2</sub> further collides with a HIO<sub>2</sub> monomer, yielding the stable (HIO<sub>2</sub>)<sub>3</sub>(MSA)<sub>2</sub> cluster against evaporation. As to HIO<sub>3</sub>-HIO<sub>2</sub>-MSA nucleation, the formation of (HIO<sub>3</sub>)<sub>1</sub>(HIO<sub>2</sub>)<sub>3</sub>(MSA)<sub>1</sub> cluster arises from i) the collision of (HIO<sub>2</sub>)<sub>2</sub>(MSA)<sub>1</sub> with (HIO<sub>3</sub>)<sub>1</sub>(HIO<sub>2</sub>)<sub>1</sub> (18%, energy barrier: 1.00 kcal mol<sup>-1</sup>), and ii) (HIO<sub>3</sub>)<sub>1</sub>(HIO<sub>2</sub>)<sub>2</sub> with (HIO<sub>2</sub>)<sub>1</sub>(MSA)<sub>1</sub> (62%, energy barrier: 0.17 kcal mol<sup>-1</sup>), as well as iii) (HIO<sub>3</sub>)<sub>1</sub>(HIO<sub>2</sub>)<sub>3</sub> binding with a MSA monomer (20%, energy barrier: 3.80 kcal mol<sup>-1</sup>). In addition, for the non-MSA pathway marked by purple arrows, 76% of (HIO<sub>3</sub>)<sub>2</sub>(HIO<sub>2</sub>)<sub>2</sub> cluster formation arises from the collision between two (HIO<sub>3</sub>)<sub>1</sub>(HIO<sub>2</sub>)<sub>1</sub> cluster, which accords closely with the barrierless pathway shown in Fig. 3(b).

(a) Cluster formation pathway



Branch ratio of flux out ( $T = 278 \text{ K}$ ,  $CS = 2.0 \times 10^{-3} \text{ s}^{-1}$ )



(b) Free energy surface of cluster formation

$T = 278 \text{ K}$ ,  $[\text{HIO}_3] = 1.0 \times 10^6$ ,  $[\text{HIO}_2] = 2.0 \times 10^4$ ,  $[\text{MSA}] = 5.0 \times 10^6 \text{ molec. cm}^{-3}$

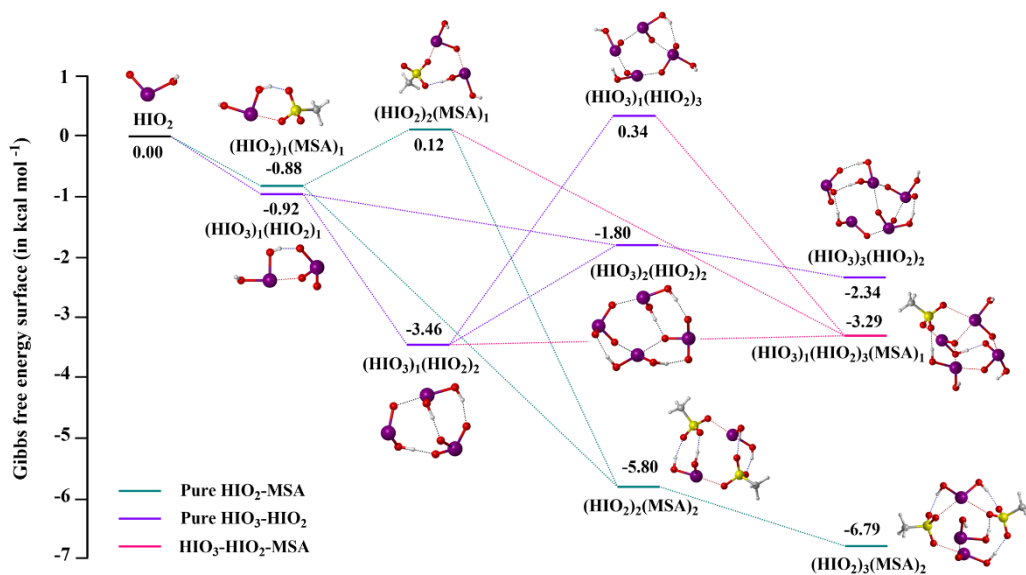


**Figure 3.** (a) Left: main cluster growth pathway of the  $\text{HIO}_3$ - $\text{HIO}_2$ -MSA nucleation system at  $T = 278\text{K}$ ,  $CS = 2.0 \times 10^{-3} \text{ s}^{-1}$ ,  $[\text{HIO}_3] = 1.0 \times 10^6$ ,  $[\text{HIO}_2] = 2.0 \times 10^4$ , and  $[\text{MSA}] = 5.0 \times 10^6 \text{ molec. cm}^{-3}$ . Right: branch ratio of flux out under varying  $[\text{MSA}]$  ( $10^6 - 10^8 \text{ molec. cm}^{-3}$ ) and  $[\text{HIO}_3]$  ( $10^6 - 10^8 \text{ molec. cm}^{-3}$ ). The yellow and purple arrows (or bar) denote MSA-involved and non-MSA flux out (or branch ratio), respectively. (b) The Gibbs free energies of cluster formation ( $\Delta G$ , kcal  $\text{mol}^{-1}$ ) based on the main clustering pathway in  $\text{HIO}_3$ - $\text{HIO}_2$ -MSA nucleation system.  $[\text{HIO}_3]/[\text{HIO}_2]$  is a constant.



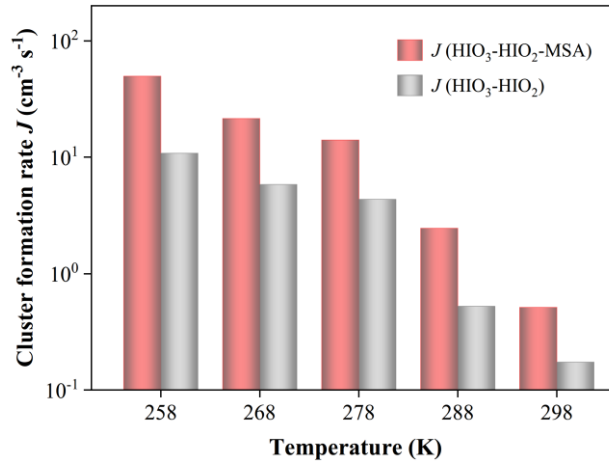
Overall, the MSA-involved pathways contribute to 74% of cluster formation, while the non-MSA path accounts for only 26%. Although the HIO<sub>3</sub>-HIO<sub>2</sub>-MSA growth pathway is less favorable than the HIO<sub>3</sub>-HIO<sub>2</sub> and HIO<sub>2</sub>-MSA pathways at  $T =$   
185 278 K, it can become barrierless at a lower temperature of 268 K (Fig. S5). This result may be explained by the fact that the lower temperature results in a decrease in the evaporation rates of the HIO<sub>3</sub>-HIO<sub>2</sub>-MSA clusters. The detailed cluster evaporation paths and corresponding  $\gamma$  at 268 K and 278 K are collected in Table S5 and Table S6. Generally, stable clusters have lower evaporation rates. According to the calculated cluster evaporation rates ( $\Sigma\gamma$ , s<sup>-1</sup>) at 278 K (Table S7), more than  
190 40% of the clusters have  $\Sigma\gamma$  less than 10<sup>-3</sup> s<sup>-1</sup>, indicating relatively high stability ( $\beta C/\Sigma\gamma > 1$ ). Among these resulting stable clusters (see Fig. S6), the majority (85%) contain HIO<sub>2</sub>. Moreover, the concentration of these stable clusters increases gradually with time, even reaching a maximum of 10<sup>4</sup> molec. cm<sup>-3</sup> (Fig. S6). Of these stable clusters, initial (HIO<sub>3</sub>)<sub>1</sub>(HIO<sub>2</sub>)<sub>1</sub>, (HIO<sub>2</sub>)<sub>2</sub>, and (MSA)<sub>1</sub>(HIO<sub>2</sub>)<sub>1</sub> dimer form rapidly, and at  $t = \sim 1$  s, heterotrimers (HIO<sub>3</sub>)<sub>1</sub>(HIO<sub>2</sub>)<sub>2</sub> and (MSA)<sub>1</sub>(HIO<sub>2</sub>)<sub>2</sub> begin to form, after which, the larger-sized clusters also form. These time-dependent evidence suggests that MSA is involved in the whole clustering process, from the initial formation of smaller clusters to the large-sized nucleated clusters that potentially further  
195 grow. Taken together, these findings highlight the direct and significant involvement of MSA in HIO<sub>3</sub>-HIO<sub>2</sub> nucleation, facilitating cluster formation.

As presented in the right of Fig. 3(a), the contribution of different clustering pathways to the flux out varies with precursor concentrations. With increasing [MSA] from 10<sup>6</sup> to 10<sup>8</sup> molec. cm<sup>-3</sup>, the contribution of MSA-involved pathways rises from 1% to 99% during nucleation. And at the median [MSA] of 10<sup>7</sup> molec. cm<sup>-3</sup>, the MSA-involved pathway contributes 86%,  
200 whereas the non-MSA pathway accounts for just 14%. In contrast, the ratio of MSA-involved pathways decreases (from 86% to 0%) with increasing concentrations of iodine oxoacids. At higher [HIO<sub>3</sub>] of 10<sup>8</sup> molec. cm<sup>-3</sup>, the HIO<sub>3</sub>-HIO<sub>2</sub> pathway dominates nucleation. Predictably, the kinetic impact of MSA on HIO<sub>3</sub>-HIO<sub>2</sub> nucleation is more pronounced in marine regions with richer MSA away from iodine sources.

### 3.3 Enhancement on Cluster Formation Rates

205 Guided by the clustering pathway analysis, MSA has shown its potential to participate in the HIO<sub>3</sub>-HIO<sub>2</sub>-based nucleation, but its detailed impacts on cluster formation rates ( $J$ , cm<sup>-3</sup> s<sup>-1</sup>) remain uncertain. Herein, the influence of MSA on  $J$  under different atmospheric conditions is systematically analyzed below.

Figure 4 presents the simulated  $J$  of HIO<sub>3</sub>-HIO<sub>2</sub>-MSA (red bar) and HIO<sub>3</sub>-HIO<sub>2</sub> system (grey bar) against the varying temperatures ( $T = 258 - 298$  K) at  $CS = 2.0 \times 10^{-3}$  s<sup>-1</sup>,  $[HIO_3] = 1.0 \times 10^7$ ,  $[HIO_2] = 2.0 \times 10^5$ , and  $[MSA] = 1.0 \times 10^7$  molec.  
210 cm<sup>-3</sup>. Clearly,  $J(\text{HIO}_3\text{-HIO}_2\text{-MSA})$  is consistently higher than  $J(\text{HIO}_3\text{-HIO}_2)$ , highlighting the enhancement of MSA on HIO<sub>3</sub>-HIO<sub>2</sub>-based clustering under common atmospheric temperatures. Specifically, both  $J(\text{HIO}_3\text{-HIO}_2\text{-MSA})$  and  $J(\text{HIO}_3\text{-HIO}_2)$  are negatively dependent on  $T$ , due to reduced cluster evaporation caused by low  $T$ . As a result, MSA could promote nucleation with higher  $J$ , especially at the colder regions, such as polar oceans.

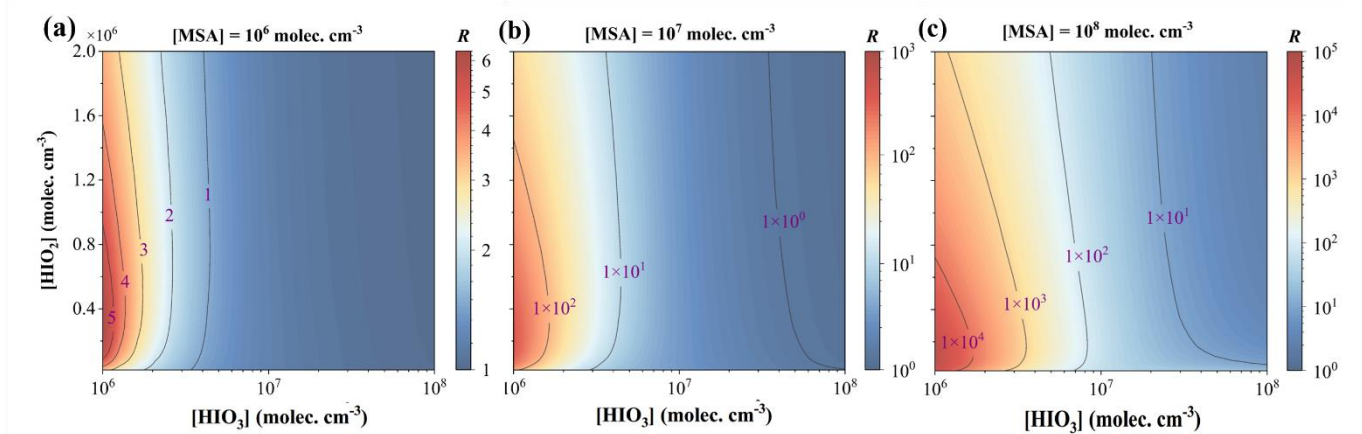


215 **Figure 4.** Simulated cluster formation rates  $J$  ( $\text{cm}^{-3} \text{s}^{-1}$ ) against varying atmospheric temperatures:  $T = 258 - 298 \text{ K}$ ,  $\text{CS} = 2.0 \times 10^{-3} \text{ s}^{-1}$ ,  
 220  $[\text{HIO}_3] = 1.0 \times 10^7$ ,  $[\text{HIO}_2] = 2.0 \times 10^5$ , and  $[\text{MSA}] = 1.0 \times 10^7 \text{ molec. cm}^{-3}$ .

It's worth noting that apart from atmospheric temperature, precursor concentrations might also vary regionally or seasonally, which can further affect nucleation. So, to comprehensively reveal the effect of MSA, here we defined and calculated MSA-driven enhancement factor  $R$  (Eq. (6)) under varying concentrations of MSA,  $\text{HIO}_3$ , and  $\text{HIO}_2$  (i.e.,  $[\text{MSA}]$ ,  
 220  $[\text{HIO}_3]$ , and  $[\text{HIO}_2]$ , unit:  $\text{molec. cm}^{-3}$ ).

$$R = \frac{J(\text{HIO}_3\text{-HIO}_2\text{-MSA})}{J(\text{HIO}_3\text{-HIO}_2)} = \frac{J([\text{HIO}_3] = x, [\text{HIO}_2] = y, [\text{MSA}] = z)}{J([\text{HIO}_3] = x, [\text{HIO}_2] = y)}, \quad (6)$$

where  $J(\text{HIO}_3\text{-HIO}_2\text{-MSA})$  and  $J(\text{HIO}_3\text{-HIO}_2)$  represent the cluster formation rate of  $\text{HIO}_3\text{-HIO}_2\text{-MSA}$  and  $\text{HIO}_3\text{-HIO}_2$  system, respectively.  $x$ ,  $y$  and  $z$  are the adopted  $[\text{HIO}_3]$ ,  $[\text{HIO}_2]$ , and  $[\text{MSA}]$ , respectively.



225 **Figure 5.** Enhancement strength  $R$  of MSA on cluster formation rates at varying precursor concentrations:  $[\text{HIO}_3] = 10^6 - 10^8$ ,  $[\text{HIO}_2] = 2.0 \times 10^4 - 2.0 \times 10^6 \text{ molec. cm}^{-3}$ , (a)  $[\text{MSA}] = 1.0 \times 10^6 \text{ molec. cm}^{-3}$ , (b)  $[\text{MSA}] = 1.0 \times 10^7 \text{ molec. cm}^{-3}$ , and (c)  $[\text{MSA}] = 1.0 \times 10^8 \text{ molec. cm}^{-3}$ ,  $T = 278 \text{ K}$ ,  $\text{CS} = 2.0 \times 10^{-3} \text{ s}^{-1}$ .

As seen from Fig. 5, with [MSA] ranging from  $10^6$  to  $10^8$  molec.  $\text{cm}^{-3}$  (Fig. 5(a) – (c)), the maximum  $R$  increases from 5 to  $10^4$ -fold, which is primarily due to MSA-mediated synergistic nucleation with  $\text{HIO}_3$  and  $\text{HIO}_2$  (recalling Sect. 3.2). Even at a median [MSA] of  $1.0 \times 10^7$  molec.  $\text{cm}^{-3}$ , the resulting  $R$  can reach approximately  $10^2$ -fold. In contrast,  $R$  is decayed at conditions of higher  $[\text{HIO}_3]$  and  $[\text{HIO}_2]$ . Furthermore, at the conditions with lower  $[\text{HIO}_3]/[\text{HIO}_2]$ , where  $R$  is higher, the contribution of MSA nucleating with  $\text{HIO}_2$  increases due to the relative scarcity of  $\text{HIO}_3$ . Conversely,  $R$  decreases at higher  $[\text{HIO}_3]/[\text{HIO}_2]$ , i.e., the impacts of MSA decreases. That is, the enhancing effect of MSA on  $J$  is limited in near-iodine source regions. Naturally, in regions with sparser iodine, the promoting effect of MSA is significant. However, the atmospheric  $[\text{HIO}_3]$  ranges widely from  $10^6$  to  $10^8$  molec.  $\text{cm}^{-3}$ . When  $[\text{HIO}_3]$  is comparable or higher than [MSA], the  $\text{HIO}_3$ - $\text{HIO}_2$  pathway contributes more, and the  $R$  of MSA decreases with the rising  $[\text{HIO}_3]$ . It is worth noting that when  $[\text{HIO}_3]$  is comparable to [MSA], the  $R$  of MSA is greater than 2, as the contribution of MSA to clustering includes not only the direct formation of  $\text{HIO}_3$ - $\text{HIO}_2$ -MSA clusters ( $\sim 20\%$ ), but also its ‘catalysis’ role in facilitating formation of initial  $\text{HIO}_3$ - $\text{HIO}_2$  clusters (Fig. S7). To sum up, MSA can promote nucleation, particularly in marine regions characterized by lower  $T$ , lower  $[\text{HIO}_3]$  and  $[\text{HIO}_2]$ . In addition, we also considered the conditions in relatively polluted ( $\text{CS} = 1.0 \times 10^{-2} \text{ s}^{-1}$ ) and clean ( $\text{CS} = 1.0 \times 10^{-4} \text{ s}^{-1}$ ) environments and found that, similar to the environment with a CS value of  $2.0 \times 10^{-3} \text{ s}^{-1}$ , MSA exhibits significant promoting effect on iodine particle formation (Figs. S8 – S11). Furthermore, the effect of  $\text{HIO}_2$  addition on the whole nucleation system was considered, as it is not only the rate-limiting step for cluster formation, leading to the significant increasement of the  $J(\text{HIO}_3$ - $\text{HIO}_2$ -MSA) compared to  $J(\text{HIO}_3$ -MSA) (Fig. S12), but also thermodynamically favorable due to  $\text{HIO}_3$ - $\text{HIO}_2$ -MSA path is almost barrierless ( $1.24 \text{ kcal mol}^{-1}$ ) compared to  $\text{HIO}_3$ -MSA pathway (Fig. S13).

### 3.4 Comparison with Field Observations

To further assess the atmospheric implication of the proposed  $\text{HIO}_3$ - $\text{HIO}_2$ -MSA nucleation, we herein simulated  $J$  in Fig. 6 based on the ambient conditions of the typical polar regions (e.g., Ny-Ålesund and Marambio) and the mid-latitude marine regions (e.g., Mace Head and Réunion). Subsequently, we compared these simulation results with observed nucleation rates and the definition of cluster formation rate was detailed in Supporting Information (SI). As shown in Fig. 6(a), the  $J(\text{HIO}_3$ - $\text{HIO}_2$ -MSA) simulated at  $T = 268 \text{ K}$ ,  $\text{CS} = 4.0 \times 10^{-4} \text{ s}^{-1}$ ,  $[\text{HIO}_3] = 10^5 - 10^6$ ,  $[\text{HIO}_2] = 2.0 \times 10^3 - 2.0 \times 10^4$ , and  $[\text{MSA}] = 10^6 - 10^8$  molec.  $\text{cm}^{-3}$  was compared with field observations in coastal Ny-Ålesund (Beck et al., 2021; He et al., 2021). Both  $J(\text{HIO}_3$ - $\text{HIO}_2$ -MSA) and  $J(\text{HIO}_3$ - $\text{HIO}_2)$  increase with the rising  $[\text{HIO}_3]$  and  $[\text{HIO}_2]$ . Importantly, the addition of MSA effectively promotes  $J$  to a higher level (orange area), aligning with most field measurements ( $1.2 \times 10^{-3} - 1.2 \times 10^{-1} \text{ cm}^{-3} \text{ s}^{-1}$ , gray lines) (Beck et al., 2021). Even when [MSA] is as low as  $1.0 \times 10^6$  molec.  $\text{cm}^{-3}$  (the orange line below), the  $J(\text{HIO}_3$ - $\text{HIO}_2$ -MSA) can be one order of magnitude higher than the observed  $J$  of  $1.2 \times 10^{-3} \text{ cm}^{-3} \text{ s}^{-1}$  (the gray line below). Moreover, the simulated  $J$  in Fig. 6(b) was obtained at the conditions of coastal Marambio, Antarctic:  $T = 273 \text{ K}$ ,  $\text{CS} = 1.0 \times 10^{-4} \text{ s}^{-1}$ ,  $[\text{HIO}_3] = 10^5 - 10^6$ ,  $[\text{HIO}_2] = 2.0 \times 10^3 - 2.0 \times 10^4$ , and  $[\text{MSA}] = 10^6 - 10^7$  molec.  $\text{cm}^{-3}$  (Quéléver et al., 2022; He et al., 2021). Compared to  $J(\text{HIO}_3$ - $\text{HIO}_2)$ , the MSA-enhanced  $J(\text{HIO}_3$ - $\text{HIO}_2$ -MSA) is overall higher, better fitting with the field observations

260  $(1.2 \times 10^{-1} - 2.4 \times 10^1 \text{ cm}^{-3} \text{ s}^{-1})$ , gray line) (Quéléver et al., 2022). These findings imply that MSA potentially plays a vital role in cold polar oceanic regions, particularly with higher [MSA] during NPF events.

In addition, the influence of  $\text{HIO}_3\text{-HIO}_2\text{-MSA}$  nucleation over the relatively warmer mid-latitude marine areas, such as Mace Head and Réunion, was investigated here (Fig. S14). We found that  $J(\text{HIO}_3\text{-HIO}_2\text{-MSA})$  is slightly higher than  $J(\text{HIO}_3\text{-HIO}_2)$ , especially at regions with high concentrations of iodine oxoacids (e.g., Mace Head), showing a relatively limited  
 265 enhancement of MSA on nucleation. Based on the simulated  $J(\text{HIO}_3\text{-HIO}_2)$  ( $\sim 1.2 \times 10^4 \text{ cm}^{-3} \text{ s}^{-1}$ ), iodine nucleation can pretty much explain the NPF events of Mace Head (Fig. S14(a)), which provides potential theoretical evidence for explaining the previous findings (Sipilä et al., 2016).

Overall, at the mid-latitude oceans, especially near iodine sources like Mace Head, MSA may have limited enhancement on nucleation. In this case, the clustering process is dominated by abundant iodine oxoacids. While in the colder polar regions,  
 270 particularly with higher [MSA] like Marambio, MSA indeed significantly facilitates  $\text{HIO}_3\text{-HIO}_2$  nucleation, suggesting a vital role in polar NPF.

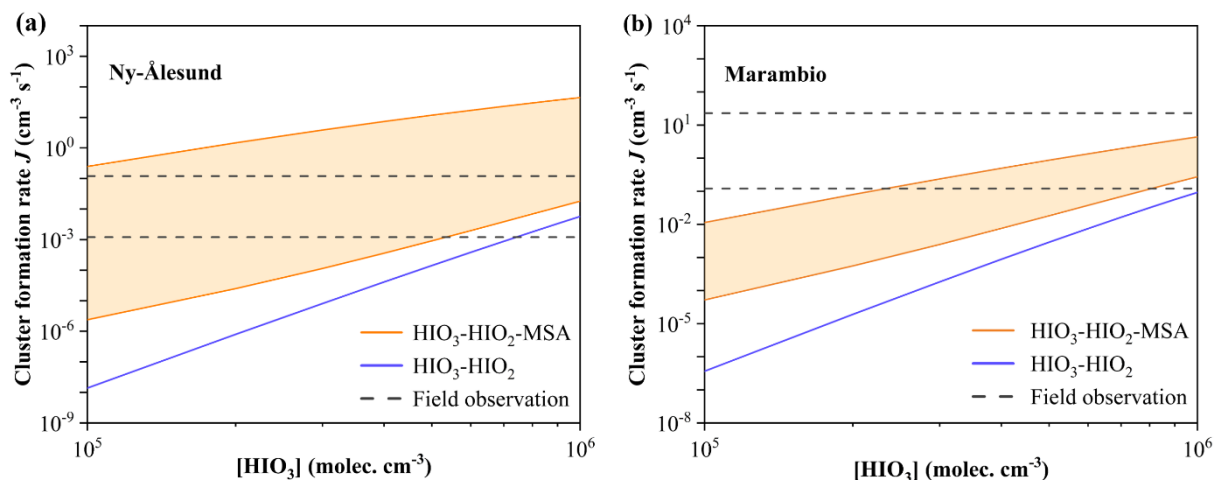


**Figure 6.** Comparison with the simulated cluster formation rates ( $J$ ,  $\text{cm}^{-3} \text{ s}^{-1}$ ) and field observations at the ambient conditions of (a) Ny-Ålesund ( $T = 268 \text{ K}$ ,  $\text{CS} = 4.0 \times 10^{-4} \text{ s}^{-1}$ ,  $[\text{HIO}_3] = 10^5 - 10^6$ ,  $[\text{HIO}_2] = 2.0 \times 10^3 - 2.0 \times 10^4$ , and  $[\text{MSA}] = 10^6 - 10^8 \text{ molec. cm}^{-3}$ ), (b)  
 275 Marambio ( $T = 273 \text{ K}$ ,  $\text{CS} = 1.0 \times 10^{-4} \text{ s}^{-1}$ ,  $[\text{HIO}_3] = 10^5 - 10^6$ ,  $[\text{HIO}_2] = 2.0 \times 10^3 - 2.0 \times 10^4$ , and  $[\text{MSA}] = 10^6 - 10^7 \text{ molec. cm}^{-3}$ ). The orange area, blue line and gray line represent  $J(\text{HIO}_3\text{-HIO}_2\text{-MSA})$ ,  $J(\text{HIO}_3\text{-HIO}_2)$ , and  $J(\text{Field observation})$ , respectively.  $[\text{HIO}_3]/[\text{HIO}_2]$  is a constant.

#### 4 Conclusion

The present study systematically investigates the  $\text{HIO}_3\text{-HIO}_2$ -based nucleation process enhanced by MSA at the molecular  
 280 level by QC calculations and ACDC simulations. The results indicate that MSA can stabilize  $\text{HIO}_3\text{-HIO}_2$ -based clusters by

building the intricate networks with more HBs and XBs. During clustering, MSA replaces  $\text{HIO}_3$  in protonating  $\text{HIO}_2$  to form ion pairs, resulting in relatively strong electrostatic attractions. In addition, thermodynamic analyses suggest that MSA-involved clustering is nearly barrierless. Compared to the  $\text{HIO}_3$ - $\text{HIO}_2$  system reported previously, the MSA-involved synergistic nucleation with  $\text{HIO}_3$  and  $\text{HIO}_2$  proceeds more efficiently, through two additional clustering pathways: i)  $\text{HIO}_2$ -MSA binary and ii)  $\text{HIO}_3$ - $\text{HIO}_2$ -MSA ternary pathway. Moreover, the resulting enhancement of MSA on nucleation is more substantial at colder regions, especially with richer MSA, but weaker in the environments near iodine source. Further comparison with field observations indicates that the  $\text{HIO}_3$ - $\text{HIO}_2$ -MSA synergistic nucleation plays a limited role in mid-latitude ocean regions, particularly in regions with abundant iodine (e.g., Mace Head), but a potential role in colder polar regions (e.g., Ny-Ålesund and Marambio).

285  
290 This study highlights the essential enhancing role of MSA in iodine oxoacids nucleation, and the  $\text{HIO}_3$ - $\text{HIO}_2$ -MSA synergistic nucleation may help to explain the observation of abundant iodine particles during marine NPF events. Given the complex oceanic atmosphere, other potential nucleation precursors beyond MSA, such as sulfuric acid and amines, may also affect the  $\text{HIO}_3$ - $\text{HIO}_2$  nucleation process and further contribute to the formation of marine iodine particles, which deserves future investigations.

295 **Data availability.** The data in this article are available from the corresponding author upon request (anning@bit.edu.cn and zhangxiuhui@bit.edu.cn).

**Supplement.** The supplement related to this article is available online at :

**Author contribution.** XZ designed and supervised the research. JL and NW performed the quantum chemical calculations and the ACDC simulations. JL, NW, BC and AN analyzed data. JL, AN and XZ wrote the paper with contributions from all  
300 of the other co-authors.

**Competing interests.** The contact author has declared that neither they nor their co-authors have any competing interests.

**Disclaimer.** Publisher's note: Copernicus Publications remains neutral with regard to jurisdictional claims in published maps and institutional affiliations.

**Acknowledgement.** We acknowledge the National Supercomputing Center in Shenzhen for providing the computational  
305 resources and the TURBOMOLE program.

**Financial support.** This work is supported by the National Science Fund for Distinguished Young Scholars (grant no. 22225607), and the National Natural Science Foundation of China (grant nos. 21976015, 22306011, and 22122610). An Ning was supported by the China Postdoctoral Science Foundation (grant no. 2023M730236).

## 310 **References**

- Ahlrichs, R., Bär, M., Häser, M., Horn, H. and Kölmel, C.: Electronic structure calculations on workstation computers: The program system turbomole, *Chem. Phys. Lett.*, 162, 165–169, [http://doi.org/10.1016/0009-2614\(89\)85118-8](http://doi.org/10.1016/0009-2614(89)85118-8), 1989.
- Almeida, J., Schobesberger, S., Kürten, A., Ortega, I. K., Kupiainen-Määttä, O., Praplan, A. P., Adamov, A., Amorim, A., Bianchi, F., Breitenlechner, M., David, A., Dommen, J., Donahue, N. M., Downard, A., Dunne, E., Duplissy, J., Ehrhart, S., Flagan, R. C., Franchin, A., Guida, R., Hakala, J., Hansel, A., Heinritzi, M., Henschel, H., Jokinen, T., Junninen, H., Kajos, M., Kangasluoma, J., Keskinen, H., Kupc, A., Kurten, T., Kvashin, A. N., Laaksonen, A., Lehtipalo, K., Leiminger, M., Leppä, J., Loukonen, V., Makhmutov, V., Mathot, S., McGrath, M. J., Nieminen, T., Olenius, T., Onnela, A., Petäjä,
- 315

- T., Riccobono, F., Riipinen, I., Rissanen, M., Rondo, L., Ruuskanen, T., Santos, F. D., Sarnela, N., Schallhart, S., Schnitzhofer, R., Seinfeld, J. H., Simon, M., Sipilä, M., Stozhkov, Y., Stratmann, F., Tomé, A., Tröstl, J., Tsagkogeorgas, G., Vaattovaara, P., Viisanen, Y., Virtanen, A., Vrtala, A., Wagner, P. E., Weingartner, E., Wex, H., Williamson, C., Wimmer, D., Ye, P., Yli-Juuti, T., Carslaw, K. S., Kulmala, M., Curtius, J., Baltensperger, U., Worsnop, D. R., Vehkamäki, H. and Kirkby, J.: Molecular understanding of sulphuric acid-amine particle nucleation in the atmosphere, *Nature*, 502, 359–363, <http://doi.org/10.1038/nature12663>, 2013.
- 320 Baccarini, A., Karlsson, L., Dommen, J., Duplessis, P., Vullers, J., Brooks, I. M., Saiz-Lopez, A., Salter, M., Tjernstrom, M., Baltensperger, U., Zieger, P. and Schmale, J.: Frequent new particle formation over the high Arctic pack ice by enhanced iodine emissions, *Nat. Commun.*, 11, 4924, <http://doi.org/10.1038/s41467-020-18551-0>, 2020.
- 325 Beck, L. J., Sarnela, N., Junninen, H., Hoppe, C. J. M., Garmash, O., Bianchi, F., Riva, M., Rose, C., Peräkylä, O., Wimmer, D., Kausiala, O., Jokinen, T., Ahonen, L., Mikkilä, J., Hakala, J., He, X. C., Kontkanen, J., Wolf, K. K. E., Cappelletti, D., Mazzola, M., Traversi, R., Petroselli, C., Viola, A. P., Vitale, V., Lange, R., Massling, A., Nøjgaard, J. K., Krejci, R., 330 Karlsson, L., Zieger, P., Jang, S., Lee, K., Vakkari, V., Lampilahti, J., Thakur, R. C., Leino, K., Kangasluoma, J., Duplissy, E. M., Siivola, E., Marbouti, M., Tham, Y. J., Saiz-Lopez, A., Petäjä, T., Ehn, M., Worsnop, D. R., Skov, H., Kulmala, M., Kerminen, V. M. and Sipilä, M.: Differing Mechanisms of New Particle Formation at Two Arctic Sites, *Geophys. Res. Lett.*, 48, <http://doi.org/10.1029/2020gl091334>, 2021.
- 335 Berresheim, H., Elste, T., Rosman, K., Dal Maso, M., Tremmel, H. G., Mäkelä, J. M., Allen, A. G., Kulmala, M. and Hansson, H.-C.: Gas-aerosol relationships of H<sub>2</sub>SO<sub>4</sub>, MSA, and OH: Observations in the coastal marine boundary layer at Mace Head, Ireland, *J. Geophys. Res.-Atmos.*, 107, PAR 5-1–PAR 5-12, <http://doi.org/10.1029/2000jd000229>, 2002.
- Bork, N., Elm, J., Olenius, T. and Vehkamäki, H.: Methane sulfonic acid-enhanced formation of molecular clusters of sulfuric acid and dimethyl amine, *Atmos. Chem. Phys.*, 14, 12023–12030, <http://doi.org/10.5194/acp-14-12023-2014>, 2014.
- Brean, J., Dall’Osto, M., Simó, R., Shi, Z., Beddows, D. C. S. and Harrison, R. M.: Open ocean and coastal new particle 340 formation from sulfuric acid and amines around the Antarctic Peninsula, *Nat. Geosci.*, 14, 383–388, <http://doi.org/10.1038/s41561-021-00751-y>, 2021.
- Chen, L., Wang, J., Gao, Y., Xu, G., Yang, X., Lin, Q. and Zhang, Y.: Latitudinal distributions of atmospheric MSA and MSA/nss-SO<sub>4</sub><sup>2-</sup> ratios in summer over the high latitude regions of the Southern and Northern Hemispheres, *J. Geophys. Res.-Atmos.*, 117, <http://doi.org/10.1029/2011jd016559>, 2012.
- 345 Chen, Q., Sherwen, T., Evans, M. and Alexander, B.: DMS oxidation and sulfur aerosol formation in the marine troposphere: a focus on reactive halogen and multiphase chemistry, *Atmos. Chem. Phys.*, 18, 13617–13637, <http://doi.org/10.5194/acp-18-13617-2018>, 2018.
- Dal Maso, M., Kulmala, M., Lehtinen, K. E. J., Mäkelä, J. M., Aalto, P. and O’Dowd, C. D.: Condensation and coagulation sinks and formation of nucleation mode particles in coastal and boreal forest boundary layers, *J. Geophys. Res.-Atmos.*, 350 107, PAR 2-1–PAR 2-10, <http://doi.org/10.1029/2001jd001053>, 2002.

- Eisele, F. L. and Tanner, D. J.: Measurement of the gas phase concentration of H<sub>2</sub>SO<sub>4</sub> and methane sulfonic acid and estimates of H<sub>2</sub>SO<sub>4</sub> production and loss in the atmosphere, *J. Geophys. Res.*, 98, 9001–9010, <http://doi.org/10.1029/93JD00031>, 1993.
- 355 Francl, M. M., Pietro, W. J., Hehre, W. J., Binkley, J. S., Gordon, M. S., DeFrees, D. J. and Pople, J. A.: Self-consistent molecular orbital methods. XXIII. A polarization-type basis set for second-row elements, *J. Chem. Phys.*, 77, 3654–3665, <http://doi.org/10.1063/1.444267>, 1982.
- Frisch, M. J., Trucks, G. W., Schlegel, H. B., Scuseria, G. E., Robb, M. A., Cheeseman, J. R., Scalmani, G., Barone, V., Mennucci, B., Petersson, G. A., Nakatsuji, H., Caricato, M., Li, X., Hratchian, H. P., Izmaylov, A. F., Bloino, J., Zheng, G., Sonnenberg, J. L., Hada, M., Ehara, M., Toyota, K., Fukuda, R., Hasegawa, J., Ishida, M., Nakajima, T., Honda, Y., Kitao, O., Nakai, H., Vreven, T., Montgomery, J. A., Peralta, J. E., Ogliaro, F., Bearpark, M., Heyd, J. J., Brothers, E.,  
360 Kudin, K. N., Staroverov, V. N., Kobayashi, R., Normand, J., Raghavachari, K., Rendell, A., Burant, J. C., Iyengar, S. S., Tomasi, J., Cossi, M., Rega, N., Millam, J. M., Klene, M., Knox, J. E., Cross, J. B., Bakken, V., Adamo, C., Jaramillo, J., Gomperts, R., Stratmann, R. E., Yazyev, O., Austin, A. J., Cammi, R., Pomelli, C., Ochterski, J. W., Martin, R. L., Morokuma, K., Zakrzewski, V. G., Voth, G. A., Salvador, P., Dannenberg, J. J., Dapprich, S., Daniels, A. D., Farkas, O., Foresman, J. B., Ortiz, J. V., Cioslowski, J. and Fox, D. J.: Gaussian 09, Revision A.02, Gaussian Inc, Wallingford CT,  
365 <https://gaussian.com/g09citation/> (last access: 07 May 2022), 2009.
- Grabowski, S. J.: Hydrogen bonding strength—measures based on geometric and topological parameters, *J. Phys. Org. Chem.*, 17, 18–31, <http://doi.org/10.1002/poc.685>, 2004.
- Hättig, C. and Weigend, F.: CC2 excitation energy calculations on large molecules using the resolution of the identity approximation, *J. Chem. Phys.*, 113, 5154–5161, <http://doi.org/10.1063/1.1290013>, 2000.
- 370 He, X.-C., Tham, Y. J., Dada, L., Wang, M., Finkenzeller, H., Stolzenburg, D., Iyer, S., Simon, M., Irten, A. K., Shen, J., Roerup, B., Rissanen, M., Schobesberger, S., Baalbaki, R., Wang, D. S., Koenig, T. K., Jokinen, T., Sarnela, N., Beck, L. J., Almeida, J., Amanatidis, S., Amorim, A., Ataei, F., Baccarini, A., Bertozzi, B., Bianchi, F., Brilke, S., Caudillo, L., Chen, D., Chiu, R., Chu, B., Dias, A., Ding, A., Dommen, J., Duplissy, J., Haddad, I. E., Carracedo, L. G., Granzin, M., Hansel, A., Heinritzi, M., Hofbauer, V., Junninen, H., Kangasluoma, J., Kuppinen, D., Kim, C., Kong, W., Krechmer, J. E., Kuvshinov, A., Laitinen, T., Lamkaddam, H., Lee, C. P., Lehtipalo, K., Leiminger, M., Li, Z., Makhmutov, V.,  
375 Manninen, H. E., Marie, G., Marten, R., Mathot, S., Mauldin, R. L., Mentler, B., Moehler, O., Mueller, T., Nie, W., Onnela, A., Petaja, T., Pfeifer, J., Philippov, M., Ranjithkumar, A., Saiz-Lopez, A., Salma, I., Scholz, W., Schuchmann, S., Schulze, B., Steiner, G., Stozhkov, Y., Tauber, C., Tome, A., Thakur, R. C., Vaisanen, O., Vazquez-Pufleau, M., Wagner, A. C., Wang, Y., Weber, S. K., Winkler, P. M., Wu, Y., Xiao, M., Yan, C., Ye, Q., Ylisirnio, A., Zauner-Wieczorek, M., Zha, Q.,  
380 Zhou, P., Flagan, R. C., Curtius, J., Baltensperger, U., Kulmala, M., Kerminen, V.-M., Kurten, T., Donahue, N. M., Volkamer, R., Kirkby, J., Worsnop, D. R. and Sipila, M.: Role of iodine oxoacids in atmospheric aerosol nucleation, *Science*, 371, 589–595, <http://doi.org/10.1126/science.abe0298>, 2021.
- Koch, U. and Popelier, P. L. A.: Characterization of C-H-O Hydrogen Bonds on the Basis of the Charge Density, *J. Phys. Chem.*, 99, 9747–9754, <http://doi.org/10.1021/j100024a016>, 1995.



- 385 Kulmala, M., Kontkanen, J., Junninen, H., Lehtipalo, K., Manninen, H. E., Nieminen, T., Petäjä, T., Sipilä, M., Schobesberger, S., Rantala, P., Franchin, A., Jokinen, T., Järvinen, E., Äijälä, M., Kangasluoma, J., Hakala, J., Aalto, P. P., Paasonen, P., Mikkilä, J., Vanhanen, J., Aalto, J., Hakola, H., Makkonen, U., Ruuskanen, T., Mauldin, R. L., 3rd, Duplissy, J., Vehkamäki, H., Bäck, J., Kortelainen, A., Riipinen, I., Kurtén, T., Johnston, M. V., Smith, J. N., Ehn, M., Mentel, T. F., Lehtinen, K. E., Laaksonen, A., Kerminen, V. M. and Worsnop, D. R.: Direct observations of atmospheric aerosol nucleation, *Science*, 390, 339, 943–946, <http://doi.org/10.1126/science.1227385>, 2013.
- Kürten, A., Li, C., Bianchi, F., Curtius, J., Dias, A., Donahue, N. M., Duplissy, J., Flagan, R. C., Hakala, J., Jokinen, T., Kirkby, J., Kulmala, M., Laaksonen, A., Lehtipalo, K., Makhmutov, V., Onnela, A., Rissanen, M. P., Simon, M., Sipilä, M., Stozhkov, Y., Tröstl, J., Ye, P. and McMurry, P. H.: New particle formation in the sulfuric acid–dimethylamine–water system: reevaluation of CLOUD chamber measurements and comparison to an aerosol nucleation and growth model, *Atmos. Chem. Phys.*, 18, 845–863, <http://doi.org/10.5194/acp-18-845-2018>, 2018.
- Lane, J. R., Contreras-García, J., Piquemal, J. P., Miller, B. J. and Kjaergaard, H. G.: Are Bond Critical Points Really Critical for Hydrogen Bonding?, *J. Chem. Theory Comput.*, 9, 3263–3266, <http://doi.org/10.1021/ct400420r>, 2013.
- Lee, S. H., Gordon, H., Yu, H., Lehtipalo, K., Haley, R., Li, Y. and Zhang, R.: New Particle Formation in the Atmosphere: From Molecular Clusters to Global Climate, *J. Geophys. Res.-Atmos.*, 124, 7098–7146, 400 <http://doi.org/10.1029/2018jd029356>, 2019.
- Liu, L., Li, S., Zu, H. and Zhang, X.: Unexpectedly significant stabilizing mechanism of iodous acid on iodic acid nucleation under different atmospheric conditions, *Sci. Total Environ.*, 859, 159832, <http://doi.org/10.1016/j.scitotenv.2022.159832>, 2023.
- Liu, Y., Xie, H.-B., Ma, F., Chen, J. and Elm, J.: Amine-Enhanced Methanesulfonic Acid-Driven Nucleation: Predictive Model and Cluster Formation Mechanism, *Environ. Sci. Technol.*, 56, 7751–7760, <http://doi.org/10.1021/acs.est.2c01639>, 2022.
- Lu, T. and Chen, F.: Multiwfn: a multifunctional wavefunction analyzer, *J. Comput. Chem.*, 33, 580–592, <http://doi.org/10.1002/jcc.22885>, 2012.
- Lu, T. and Chen, Q.: Shermo: A general code for calculating molecular thermochemistry properties, *Comput. Theor. Chem.*, 1200, <http://doi.org/10.1016/j.comptc.2021.113249>, 2021.
- 410 Lu, Y., Liu, L., Ning, A., Yang, G., Liu, Y., Kurtén, T., Vehkamäki, H., Zhang, X. and Wang, L.: Atmospheric Sulfuric Acid-Dimethylamine Nucleation Enhanced by Trifluoroacetic Acid, *Geophys. Res. Lett.*, 47, <http://doi.org/10.1029/2019gl085627>, 2020.
- Ma, F., Xie, H. B., Zhang, R., Su, L., Jiang, Q., Tang, W., Chen, J., Engsvang, M., Elm, J. and He, X. C.: Enhancement of Atmospheric Nucleation Precursors on Iodic Acid-Induced Nucleation: Predictive Model and Mechanism, *Environ. Sci. Technol.*, 57, 6944–6954, <http://doi.org/10.1021/acs.est.3c01034>, 2023.
- 415 McGrath, M. J., Olenius, T., Ortega, I. K., Loukonen, V., Paasonen, P., Kurtén, T., Kulmala, M. and Vehkamäki, H.: Atmospheric Cluster Dynamics Code: a flexible method for solution of the birth-death equations, *Atmos. Chem. Phys.*, 12, 2345–2355, <http://doi.org/10.5194/acp-12-2345-2012>, 2012.

- Ning, A., Liu, L., Ji, L. and Zhang, X.: Molecular-level nucleation mechanism of iodic acid and methanesulfonic acid, *Atmos. Chem. Phys.*, 22, 6103–6114, <http://doi.org/10.5194/acp-22-6103-2022>, 2022.
- O'Dowd, C. D., Hämeri, K., Mäkelä, J. M., Pirjola, L., Kulmala, M., Jennings, S. G., Berresheim, H., Hansson, H.-C., Leeuw, G. d., Kunz, G. J., Allen, A. G., Hewitt, C. N., Jackson, A., Viisanen, Y. and Hoffmann, T.: A dedicated study of New Particle Formation and Fate in the Coastal Environment (PARFORCE): Overview of objectives and achievements, *J. Geophys. Res.-Atmos.*, 107, PAR 1-1–PAR 1-16, <http://doi.org/10.1029/2001jd000555>, 2002.
- O'Dowd, C. D. and Leeuw, G. d.: Marine aerosol production: a review of the current knowledge, *Philos. T. R. Soc. A* 365, 1753–1774, <http://doi.org/10.1098/rsta.2007.2043>, 2007.
- Peterson, K. A., Figgen, D., Goll, E., Stoll, H. and Dolg, M.: Systematically convergent basis sets with relativistic pseudopotentials. II. Small-core pseudopotentials and correlation consistent basis sets for the post-d group 16–18 elements, *J. Chem. Phys.*, 119, 11113–11123, <http://doi.org/10.1063/1.1622924>, 2003.
- Pöschl, U.: Atmospheric aerosols: composition, transformation, climate and health effects, *Angew. Chem. Int. Ed.*, 44, 7520–4750, <http://doi.org/10.1002/anie.200501122>, 2005.
- Quéléver, L. L. J., Dada, L., Asmi, E., Lampilahti, J., Chan, T., Ferrara, J. E., Copes, G. E., Pérez-Fogwill, G., Barreira, L., Aurela, M., Worsnop, D. R., Jokinen, T. and Sipilä, M.: Investigation of new particle formation mechanisms and aerosol processes at Marambio Station, Antarctic Peninsula, *Atmos. Chem. Phys.*, 22, 8417–8437, <http://doi.org/10.5194/acp-22-8417-2022>, 2022.
- Read, K. A., Lewis, A. C., Bauguitte, S., Rankin, A. M., Salmon, R. A., Wolff, E. W., Saiz-Lopez, A., Bloss, W. J., Heard, D. E., Lee, J. D. and Plane, J. M. C.: DMS and MSA measurements in the Antarctic Boundary Layer: impact of BrO on MSA production, *Atmos. Chem. Phys.*, 8, 2985–2997, <http://doi.org/10.5194/acp-8-2985-2008>, 2008.
- Rong, H., Liu, J., Zhang, Y., Du, L., Zhang, X. and Li, Z.: Nucleation mechanisms of iodic acid in clean and polluted coastal regions, *Chemosphere*, 253, 126743, <http://doi.org/10.1016/j.chemosphere.2020.126743>, 2020.
- Saltzman, E. S., Savoie, D. L., Zika, R. G. and Prospero, J. M.: Methane sulfonic acid in the marine atmosphere, *J. Geophys. Res.*, 88, <http://doi.org/10.1029/JC088iC15p10897>, 1983.
- Shen, J., Elm, J., Xie, H.-B., Chen, J., Niu, J. and Vehkamäki, H.: Structural Effects of Amines in Enhancing Methanesulfonic Acid-Driven New Particle Formation, *Environ. Sci. Technol.*, 54, 13498–13508, <http://doi.org/10.1021/acs.est.0c05358>, 2020.
- Shen, J., Xie, H.-B., Elm, J., Ma, F., Chen, J. and Vehkamäki, H.: Methanesulfonic Acid-driven New Particle Formation Enhanced by Monoethanolamine: A Computational Study, *Environ. Sci. Technol.*, 53, 14387–14397, <http://doi.org/10.1021/acs.est.9b05306>, 2019.
- Sipilä, M., Sarnela, N., Jokinen, T., Henschel, H., Junninen, H., Kontkanen, J., Richters, S., Kangasluoma, J., Franchin, A., peräkylä, O., Rissanen, M. P., Ehn, M., Vehkamäki, H., Kurten, T., Berndt, T., Petäjä, T., Worsnop, D., Ceburnis, D., Kerminen, V. M., Kulmala, M. and O'Dowd, C.: Molecular-scale evidence of aerosol particle formation via sequential addition of HIO<sub>3</sub>, *Nature*, 537, 532–534, <http://doi.org/10.1038/nature19314>, 2016.

- Vehkamäki, H.: *Classical Nucleation Theory in Multicomponent Systems*, Springer Science & Business Media, <https://link.springer.com/book/10.1007/1003-1540-31218-31218>, 2006.
- 455 Wang, L., Khalizov, A. F., Zheng, J., Xu, W., Ma, Y., Lal, V. and Zhang, R.: Atmospheric nanoparticles formed from heterogeneous reactions of organics, *Nat. Geosci.*, 3, 238–242, <http://doi.org/10.1038/ngeo778>, 2010.
- Wu, N., Ning, A., Liu, L., Zu, H., Liang, D. and Zhang, X.: Methanesulfonic acid and iodous acid nucleation: a novel mechanism for marine aerosols, *Phys. Chem. Chem. Phys.*, 25, 16745–16752, <http://doi.org/10.1039/d3cp01198d>, 2023.
- 460 Yan, J., Jung, J., Zhang, M., Xu, S., Lin, Q., Zhao, S. and Chen, L.: Significant Underestimation of Gaseous Methanesulfonic Acid (MSA) over Southern Ocean, *Environ. Sci. Technol.*, 53, 13064–13070, <http://doi.org/10.1021/acs.est.9b05362>, 2019.
- Yu, H., Ren, L., Huang, X., Xie, M., He, J. and Xiao, H.: Iodine speciation and size distribution in ambient aerosols at a coastal new particle formation hotspot in China, *Atmos. Chem. Phys.*, 19, 4025–4039, <http://doi.org/10.5194/acp-19-4025-2019>, 2019.
- Zhang, R.: Getting to the Critical Nucleus of Aerosol Formation, *Science*, 328, 1366–1367, 465 <http://doi.org/10.1126/science.1189732>, 2010.
- Zhang, R., Khalizov, A., Wang, L., Hu, M. and Xu, W.: Nucleation and growth of nanoparticles in the atmosphere, *Chem. Rev.*, 112, 1957–2011, <http://doi.org/10.1021/cr2001756>, 2012.
- Zhang, R., Xie, H. B., Ma, F., Chen, J., Iyer, S., Simon, M., Heinritzi, M., Shen, J., Tham, Y. J., Kurtén, T., Worsnop, D. R., Kirkby, J., Curtius, J., Sipilä, M., Kulmala, M. and He, X. C.: Critical Role of Iodous Acid in Neutral Iodine Oxoacid 470 Nucleation, *Environ. Sci. Technol.*, 56, 14166–14177, <http://doi.org/10.1021/acs.est.2c04328>, 2022a.
- Zhang, S., Li, S., Ning, A., Liu, L. and Zhang, X.: Iodous acid - a more efficient nucleation precursor than iodic acid, *Phys. Chem. Chem. Phys.*, 24, 13651–13660, <http://doi.org/10.1039/d2cp00302c>, 2022b.